



# Io's Volcanic Activity from Time Domain Adaptive Optics Observations: 2013–2018

Katherine de Kleer<sup>1</sup>, Imke de Pater<sup>2</sup>, Edward M. Molter<sup>2</sup>, Elizabeth Banks<sup>3</sup>, Ashley Gerard Davies<sup>4</sup>, Carlos Alvarez<sup>5</sup>, Randy Campbell<sup>5</sup>, Joel Aycock<sup>5</sup>, John Pelletier<sup>5</sup>, Terry Sticker<sup>5</sup>, Glenn G. Kacprzak<sup>6</sup>, Nikole M. Nielsen<sup>6</sup>, Daniel Stern<sup>4</sup>, and Joshua Tollefson<sup>2</sup>

<sup>1</sup> California Institute of Technology, 1200 E California Blvd. M/C 150-21, Pasadena, CA 91125, USA; [dekleer@caltech.edu](mailto:dekleer@caltech.edu)

<sup>2</sup> University of California, Berkeley, Berkeley, CA, USA

<sup>3</sup> The Pembroke Hill High School, Kansas City, MO, USA

<sup>4</sup> Jet Propulsion Laboratory, California Institute of Technology, Pasadena, CA, USA

<sup>5</sup> W.M. Keck Observatory, Waimea, HI, USA

<sup>6</sup> Swinburne University of Technology, Hawthorn, Victoria, Australia

Received 2019 January 26; revised 2019 May 13; accepted 2019 May 14; published 2019 June 21

## Abstract

We present measurements of the near-infrared brightness of Io's hot spots derived from 2 to 5  $\mu\text{m}$  imaging with adaptive optics on the Keck and Gemini N telescopes. The data were obtained on 271 nights between 2013 August and the end of 2018, and include nearly 1000 detections of over 75 unique hot spots. The 100 observations obtained between 2013 and 2015 have been previously published in de Kleer & de Pater the observations since the start of 2016 are presented here for the first time, and the analysis is updated to include the full five-year data set. These data provide insight into the global properties of Io's volcanism. Several new hot spots and bright eruptions have been detected, and the preference for bright eruptions to occur on Io's trailing hemisphere noted in the 2013–2015 data is strengthened by the larger data set and remains unexplained. The program overlapped in time with *Sprint-A/EXCEED* and *Juno* observations of the Jovian system, and correlations with transient phenomena seen in other components of the system have the potential to inform our understanding of the impact of Io's volcanism on Jupiter and its neutral/plasma environment.

**Key words:** infrared: planetary systems – methods: observational – planets and satellites: surfaces

**Supporting material:** machine-readable tables

## 1. Introduction

Io's dramatic volcanic activity exhibits a high degree of spatial and temporal variability. The distribution of volcanic thermal emission in space and time contains information on the underlying volcanic advection processes, providing a window into the nature of Io's geological processes as well as into how tidal heating impacts the characteristics of the volcanism it powers.

While some of Io's volcanoes have remained persistently active since the *Voyager* flybys in 1979, numerous transient eruptions appear and subside in a matter of days, hours, or even minutes (e.g., Johnson et al. 1988; Veeder et al. 1994; de Kleer et al. 2014; de Pater et al. 2014; Tsang et al. 2014; Davies et al. 2018). The timeline of thermal activity for a given volcano is indicative of the style of volcanism and hence geological processes active at that site (Davies et al. 2010). The time intervals between eruptions at a given site can provide information on characteristic resupply timescales, while a comparison of eruption timing between sites has the potential to illuminate eruption clustering if present. Finally, the periodic forcing of Io may translate into specific temporal signatures that may be apparent in thermal timelines.

Volcanoes are also distributed nonrandomly across Io's surface, showing in particular a dearth of activity at the sub- and anti-Jovian longitudes, as well as in polar regions (Hamilton et al. 2013; Veeder et al. 2015; de Kleer & de Pater 2016b), although no data set published to date has had good coverage of the high latitudes. The spatial distribution of Io's surface heat flow may place constraints on models for tidal heat dissipation in Io's interior, or may indicate the degree of fluid flow in Io's mantle through the amount of smoothing in

the observed spatial trends relative to the expected patterns. Without allowing for lateral movement of melt, the end-member case of heat deposition in a shallow aesthenosphere predicts higher heat flow at lower latitudes with the greatest heat flow centered at the sub-Jovian and anti-Jovian regions. In contrast, the end-member case of deep mantle heating results in enhanced heat flow at the poles (Gaskell et al. 1988; Segatz et al. 1988).

Determining the temporal and spatial distribution of Io's volcanism requires a large sample size of hot spot detections over a range of timescales. We have been building up a database of thermal emission from individual volcanoes on Io's surface since 2013, when we initiated a time domain campaign of adaptive optics imaging of Io's volcanoes at the Keck and Gemini N telescopes. Io has been observed using adaptive optics on Keck since 2001 (Marchis et al. 2002), but only since 2013 has there been a dedicated Io observing program at such high cadence. These observations spatially resolve Io, permitting the identification of individual active volcanoes, and are often made at multiple wavelengths in the 2–5  $\mu\text{m}$  range in order to constrain temperature and total power output. The observations have a typical spatial resolution of  $\sim 100$ –500 km depending on telescope, wavelength, and sky conditions. The collective data set is well suited to an investigation into the volcanic eruption processes at individual hot spots, which requires data capturing the time evolution of the eruptions, and to identification of spatial and temporal patterns in the distribution of activity.

The prior Io data set that is most comparable in cadence, wavelength, and spatial resolution is from the *Galileo* Near-Infrared Mapping Spectrometer (NIMS; Carlson et al. 1992),

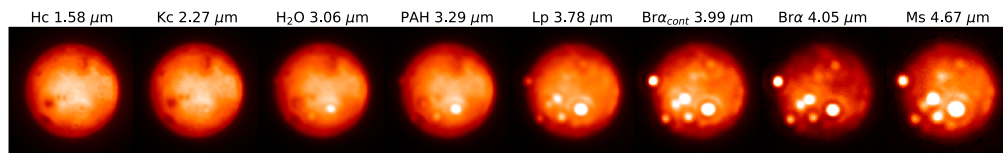


**Figure 1.** Images from Keck on 2017 May 28 demonstrating the range of filters used in the observations. All images were taken within a 30 minute window, and each is labeled with the filter name and central wavelength.

which observed Io on 25 distinct passes with a typical spatial resolution of 100–400 km on Io’s surface, including some images with resolutions as coarse as 725 km and as fine as 100 m (see Table 3.2 in Davies 2007). NIMS detected thermal emission from 115 unique hot spots (Davies et al. 2012; Veeder et al. 2012, 2015), each detected between 1 and 50+ times over the course of the mission. Long-term programs observing Io’s thermal emission from the NASA InfraRed Telescope Facility have also been very successful (Spencer et al. 1990; Veeder et al. 1994; Rathbun & Spencer 2010). While such data do not spatially resolve Io, techniques such as lucky imaging and observing Io as the satellite enters or emerges from occultation behind Jupiter have permitted brightness measurements of individual volcanoes. Though sensitive only to the brightest events and only to the Jupiter-facing hemisphere, occultation observations have by far the longest time baseline, having been made on more than 100 occasions over the past >2 decades (Rathbun et al. 2018), albeit at only one wavelength (3.5 or 3.8  $\mu\text{m}$ ).

Our spatial resolution and sensitivity to faint hot spots is intermediate between NIMS data and occultation observations, and is comparable to a typical NIMS observation. Our cadence and total number of observations are higher than all prior data sets, although the time baseline of our high cadence campaign is much shorter than the decadal timescales covered by the occultation data sets.

Our campaign is introduced in de Kleer et al. (2014), and the analysis methods and results from the first 2.5 yr of the program (100 nights of observation) are given in de Kleer & de Pater (2016a). Here we present results from the 2016–2018 observations, and a joint analysis of all data to date, 2013–2018. The flexible scheduling capabilities at Gemini N, and our Twilight Zone observing program at Keck,<sup>7</sup> have been instrumental in achieving the high cadence and quantity of observations. The observations and data analysis methods are reviewed in Section 2, the results are presented and discussed in Section 3, and the conclusions are summarized in Section 4.

## 2. Observations and Data Analysis

We observed Io in the near-infrared with adaptive optics on 271 nights between 2013 August and 2018 July; the observing dates and details are given in Table 4. Observations were made with the NIRI imager on Gemini N (Hodapp et al. 2003) combined with the ALTAIR adaptive optics system in Natural Guide Star (NGS) mode, and with the NIRC2 imager on Keck II also using NGS adaptive optics (Wizinowich et al. 2000). The Gemini N data constitute 80% of the total visits, and include images in the  $L'$  (3.78  $\mu\text{m}$ ) and  $K$ -cont (2.27  $\mu\text{m}$ ) filters. The Keck images were taken in a variety of filters from  $H$ -cont (1.58  $\mu\text{m}$ ) to  $Ms$  (4.67  $\mu\text{m}$ ), shown in Figure 1.

Images are flux calibrated to a standard star if a star was observed and the night was photometric; otherwise, the images

are calibrated to volcano-free regions of Io’s disk, which do not change measurably with time. Within each image, all hot spots are identified; their pixel locations are translated to latitude and longitude coordinates on Io’s disk based on Io’s ephemeris; and their intensity is measured based on an aperture photometry approach adapted to point sources on a bright background (de Pater et al. 2014). All observing, data reduction, and analysis procedures are described in detail in de Kleer & de Pater (2016a), and an identical approach is used here. Of the full data set, the 100 observations from 2013 through the end of 2015 were published in de Kleer & de Pater (2016a), while the 171 observations from 2016 to 2018 are presented here for the first time.

The detection limits for hot spots in the Keck and Gemini N images are given as a function of emission angle in the Appendix of de Kleer & de Pater (2016a). We use these limits to define the sensitivity of the data set as a whole to hot spots at different longitudes. This sensitivity varies by up to 20% across Io’s surface, and is used to correct the longitudinal hot spot distribution described in Section 3.4.

## 3. Results and Discussion

The coordinates, number of detections, and average brightness of each of the 75 hot spots detected and tracked by our program are listed in Table 1. The full set of near-infrared brightnesses in all filters for all 980 hot spot detections are tabulated in Table 5. In some cases, the location of a hot spot appears to shift over time or transition from one active site to another nearby; in cases where it is not clear from the data whether the emission over time is produced by a single site or multiple nearby sites, we tabulate all detections under a single site name. The timeline of  $L'$ -band (3.78  $\mu\text{m}$ ) brightness of all volcanoes is shown in Figure 2, which gives a sense for the global variability of Io’s volcanism over this period.

### 3.1. Energetic Eruptions

Since 2013 we have detected bright eruptions at 18 sites, where we define “bright” as a maximum  $L'$ -band brightness greater than 20  $\text{GW } \mu\text{m}^{-1} \text{sr}^{-1}$ . There is no hot spot on Io that consistently exhibits this level of activity, and this cutoff therefore selects for transient events. These eruptions are typically vigorous, high-power events with significant short-wavelength emission. The majority of these were short-lived, exhibiting their peak brightness for only a few days before decaying. A few volcanoes are exceptions to this rule, producing thermal emission that is consistently present at a moderate level while also exhibiting infrequent brightenings; these volcanoes are Loki Patera, Pillan Patera, Marduk Fluctus, and Kurdalagon Patera. The first three of these were active throughout the period of observation, while Kurdalagon Patera was not detected before its eruption at the beginning of 2015 but was subsequently active and variable through 2018.

<sup>7</sup> <https://www2.keck.hawaii.edu/inst/tda/TwilightZone.html>

**Table 1**  
Overview of Hot Spots

Site	Lat (°N)	Lon (°W)	$N_{\text{det}}$	$\bar{F}_{\text{filt}}^a$ (GW $\mu\text{m}^{-1}$ sr $^{-1}$ )	Filter <sup>a</sup>
Nusku Patera	-65.0	6.2	1		Narrowband Only
Uta	-34.4	21.0	57	3.6	<i>Lp</i>
Kanehekili Fluctus	-17.0	34.5	8	1.2	<i>Lp</i>
Janus Patera	-3.9	37.4	84	4.7	<i>Lp</i>
UP 38W	-25.3	37.7	1	1.9	<i>Ms</i>
Pfu374	-24.3	49.7	3	1.0	<i>Ms</i>
Masubi	-42.9	53.7	9	2.4	<i>Lp</i>
PFd1691	9.4	58.3	22	2.5	<i>Lp</i>
Laki-Oi Patera	-44.6	59.7	4	3.9	<i>Lp</i>
Shamshu Patera	-8.3	61.5	1	1.1	<i>Ms</i>
Tejeto Patera	-42.9	68.7	4	4.4	<i>Lp</i>
Chalybes Regio	55.4	70.2	80	9.6	<i>Lp</i>
Zal Patera	37.9	74.6	24	2.9	<i>Lp</i>
Tawhaki Patera	2.5	75.6	19	2.1	<i>Lp</i>
Ekhi Patera	-28.4	86.7	1	3.8	<i>Lp</i>
Gish Bar	15.6	89.1	18	3.4	<i>Lp</i>
Aluna Patera	41.7	90.1	2	3.2	<i>Ms</i>
P207	-36.5	91.1	1	5.0	<i>Lp</i>
Shango Patera	33.5	95.6	3	1.8	<i>Ms</i>
Itzamna Patera	-15.0	99.0	9	1.6	<i>Lp</i>
Arusha Patera	-39.6	99.0	4	3.5	<i>Lp</i>
Sigurd Patera	-5.1	99.2	8	4.4	<i>Lp</i>
P197	-46.9	107.3	11	6.2	<i>Lp</i>
Amirani	20.5	113.2	27	2.6	<i>Lp</i>
Dusura Patera	36.4	121.1	3	7.5	<i>Lp</i>
Maui Patera	18.2	125.8	2	3.2	<i>Lp</i>
P95	-10.0	127.8	2	36.5	<i>Lp</i>
Malik Patera	-32.9	129.6	9	3.1	<i>Lp</i>
UP 132W	18.4	131.6	5	3.6	<i>Lp</i>
Thor	40.6	134.7	2	1.3	<i>Ms</i>
P123	-41.9	139.2	20	4.6	<i>Lp</i>
Tupan Patera	-18.0	140.5	10	1.6	<i>Lp</i>
Surya Patera	21.2	149.4	4	2.7	<i>Lp</i>
Shamash Patera	-33.2	150.5	2	41.3	<i>Lp</i>
Sobo Fluctus	12.9	152.8	1		Narrowband Only
Prometheus	-1.5	153.3	22	2.8	<i>Lp</i>
Culann	-17.2	161.8	11	2.0	<i>Lp</i>
Zamama	18.5	173.2	3	1.2	<i>Lp</i>
Illyrikon Regio	-70.8	179.9	4	109.2	<i>Lp</i>
Sethlaus/Gabija Paterae	-50.0	198.1	6	11.6	<i>Lp</i>
Isum Patera	31.1	205.4	16	37.6	<i>Lp</i>
Marduk Fluctus	-23.7	211.1	87	10.5	<i>Lp</i>
Kurdalagon	-49.3	216.7	36	13.1	<i>Lp</i>
Unknown	53.6	217.8	1		Narrowband Only
Susanoo/Mulungu Paterae	18.6	221.0	10	4.5	<i>Lp</i>
201308C	29.1	228.0	11	555.7	<i>Lp</i>
P17	-3.5	228.8	1	1.8	<i>Lp</i>
P13	13.9	229.0	4	9.2	<i>Lp</i>
East Girru	21.3	233.5	3	4.9	<i>Lp</i>
Reiden Patera	-18.0	234.4	2	3.5	<i>Lp</i>
Pyerun Patera	-57.7	237.1	1	3.9	<i>Ms</i>
SE of Pele	-34.5	239.5	30	3.9	<i>Lp</i>
Pillan Patera	-11.3	243.7	21	7.1	<i>Lp</i>
Chors Patera	65.1	245.6	5	30.6	<i>Lp</i>
UP 254W	-37.1	254.5	2	67.7	<i>Lp</i>
Pele	-18.2	255.2	19	2.2	<i>Lp</i>
Shakuru Patera	24.8	261.7	2	2.7	<i>Lp</i>
Mithra Patera	-58.0	265.6	4	25.4	<i>Lp</i>
Svarog Patera	-51.6	269.3	3	4.1	<i>Ms</i>
Daedalus Patera	18.7	273.9	5	2.5	<i>Lp</i>
PV59	-38.2	289.7	22	6.7	<i>Lp</i>

**Table 1**  
(Continued)

Site	Lat (°N)	Lon (°W)	$N_{\text{det}}$	$\bar{F}_{\text{filt}}^a$ (GW $\mu\text{m}^{-1}$ sr $^{-1}$ )	Filter <sup>a</sup>
N Lerna Regio	-56.0	290.6	19	5.2	<i>Lp</i>
Kibero Patera	-12.5	297.1	2	11.7	<i>Lp</i>
Amaterasu Patera	38.8	304.3	13	7.6	<i>Lp</i>
Sengen Patera	-29.8	305.1	4	5.2	<i>Lp</i>
Rarog Patera	-39.2	305.4	14	29.3	<i>Lp</i>
Heno Patera	-55.6	307.5	7	70.3	<i>Lp</i>
Loki Patera	12.6	307.5	113	38.3	<i>Lp</i>
Shoshu Patera	-17.6	322.9	1	2.7	<i>Lp</i>
Tol-Ava Patera	0.7	326.5	4	4.4	<i>Lp</i>
PV170	-47.9	327.8	3	7.1	<i>Lp</i>
Fuchi Patera	28.3	328.7	1	1.0	<i>Lp</i>
Surt	44.4	334.1	2	1.2	<i>Ms</i>
Pfu1063	41.7	357.7	3	1.7	<i>Lp</i>
Paive Patera	-42.9	358.3	2	0.9	<i>Ms</i>

**Note.**

<sup>a</sup> The mean observed flux density  $\bar{F}_{\text{filt}}$  is given in the *Lp* filter if data were available in this filter, and in the *Ms* filter if no *Lp* detections were made. If no detections were made in either broadband filter, detection in narrowband only is indicated.

Table 2 lists these 18 hot spots and the brightest *L'*-band intensity measured at each during our program. Note that only the single brightest detection is given even though some volcanoes had multiple large eruptions. The full timeline for each of these hot spots can be found in Table 5. The events that occurred prior to the end of 2015 were presented in de Kleer & de Pater (2016a); our discussion here therefore focuses on eruptions detected since the beginning of 2016.

For volcanoes with detections at multiple wavelengths on a given night, we fit a Planck spectrum to estimate the temperature. All detections with measured temperatures above 800 K are given in Table 3; in total there are 32 such detections at 18 unique hot spots. These hot spots are not exactly the same set as the 18 sites where bright eruptions are seen, although there is significant overlap. While this is a small fraction of the total number of observations for which we were able to derive temperature estimates, it confirms previous findings that these high temperatures are common and widespread across a variety of volcanic styles and are not limited to outburst events (e.g., Carr 1986; Lopes-Gautier et al. 1999). However, we note that Io's active volcanoes likely exhibit a range of temperatures from near the magma temperature ( $\sim 1500$  K if the magma is basaltic) down to near the passive surface temperature ( $\sim 125$  K), and the temperatures recovered in a single temperature fit therefore do not directly represent any physical temperature (although they do serve as a lower limit on the eruption temperature). In fact, if the magma composition is the same at all of Io's volcanoes, then the best-fit temperature instead reflects the proportion of high-temperature to low-temperature emitting areas, and high fitted temperatures are indicative of volcanic eruptions vigorous enough that sufficient area is exposed at very high temperatures to yield a short-wavelength peak in thermal emission (e.g., Davies et al. 2010).

The temperatures in Table 3 are derived as in de Kleer & de Pater (2016a), using Markov Chain Monte Carlo simulations to determine the probability distribution for temperature and emitting area, from which the uncertainties are also derived.

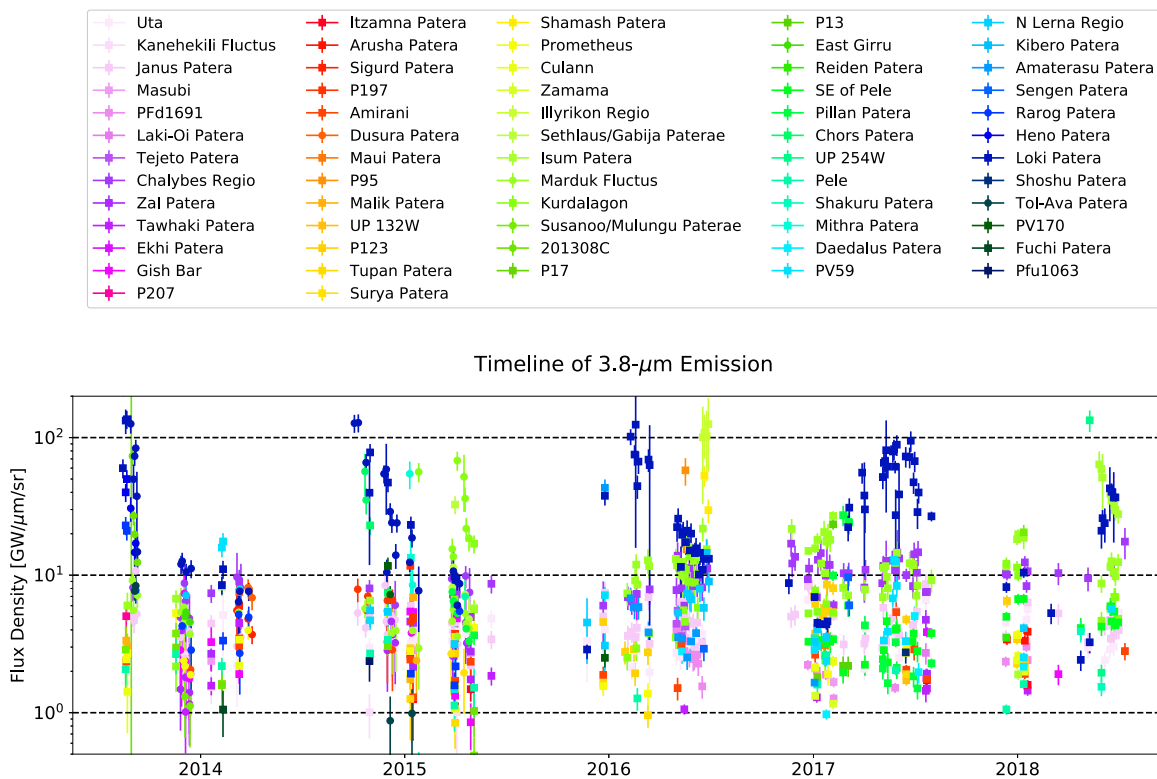


**Figure 2.** Timeline of Io’s volcanic activity from 2013 to 2018. All  $L'$ -band detections of thermal emission from volcanic centers are plotted, with each volcanic center in a different color. The gaps in the timeline correspond to periods when the Jupiter system was not observable from Maunakea. The timeline shows that there are multimonth intervals with no bright activity, and other intervals when several large eruptions took place.

Measurements from all available wavelengths are used, incorporating uncertainties on the intensity measurements, and a maximum  $K$ -cont ( $2.27 \mu\text{m}$ ) brightness limit of  $7 \text{ GW } \mu\text{m}^{-1} \text{ sr}^{-1}$  is imposed in the fitting when the hot spot was not detected at that wavelength.

The temperature estimates are derived from the intensity measurements given in Table 5, which have been corrected for geometric foreshortening. However, in the case of a high emission angle observation of an event of significant vertical extent such as fire fountaining, the short-wavelength emission may arise primarily from the hot fountaining component that is not foreshortened, while the longer-wavelength emission arises from both the fountains and the resultant lava flows, which are foreshortened. Applying the foreshortening correction across all wavelengths may therefore inflate the derived short-wavelength emission and hence the temperature, so that temperatures derived from high emission angle observations should be viewed with caution.

### 3.1.1. Eruption at P95 (2016 May)

In 2016 May a bright and short-lived eruption was detected at patera P95, near  $10^\circ\text{S } 128^\circ\text{W}$ . The eruption was first detected on May 17 with a temperature around 1000 K. The second and final detection of the eruption occurred two days later on May 19, and the eruption had already declined significantly in brightness by this time. The latest nondetection of the site prior to the eruption was May 12, while the eruption had faded to below  $I_{Lp} \sim 5 \text{ GW } \mu\text{m}^{-1} \text{ sr}^{-1}$  by May 24, and to below the detection limit even at optimal viewing geometry ( $I_{Lp} \sim 3 \text{ GW } \mu\text{m}^{-1} \text{ sr}^{-1}$ ) by May 28. While high in both temperature and infrared emission, this event therefore was short-lived,

detected only over a three-night period and constrained to be active at a detectable level for less than 16 days.

### 3.1.2. Eruptions at Shamash Patera and in the Illyrikon Regio (2016 June)

A pair of dramatic eruptions occurred in the southern hemisphere at Shamash Patera ( $33^\circ\text{S } 150^\circ\text{W}$ ) and in Illyrikon Regio near  $71^\circ\text{S } 180^\circ\text{W}$  in 2016 June. The eruption in Illyrikon Regio was first detected on June 17, and began no earlier than June 10. Shamash Patera was still not active as late as June 18, after the eruption at Illyrikon Regio had begun, but exhibited bright activity on June 20. The eruption at Shamash Patera had decayed and cooled somewhat by June 27, while the eruption in Illyrikon Regio stayed bright and hot through the end of June, after which we had no further observations until November. Figure 3 shows images of the eruptions at these volcanoes. The two volcanoes appear close in the images but are separated by over 1000 km of surface distance. The location of the hot spot in Illyrikon Regio is poorly constrained due to the high emission angle of all observations and we cannot conclusively match a surface feature at its location, but the positioning of a dark patera at  $71^\circ\text{S } 170^\circ\text{W}$  is consistent with some of the thermal emission detections, whose best-fit longitudes fall in the range of  $165^\circ\text{--}193^\circ\text{W}$ . At  $71^\circ\text{S}$ , this is the most polar hot spot detected by our program.

### 3.1.3. Eruption at UP 254W (2018 May)

On 2018 May 10, a bright, high-temperature ( $\sim 1000 \text{ K}$ ) eruption was detected at  $37^\circ\text{S } 254^\circ\text{W}$ ; a small patera at exactly this location is seen in spacecraft surface imaging (Williams et al. 2011a, 2011b) and is a plausible source of the eruption.

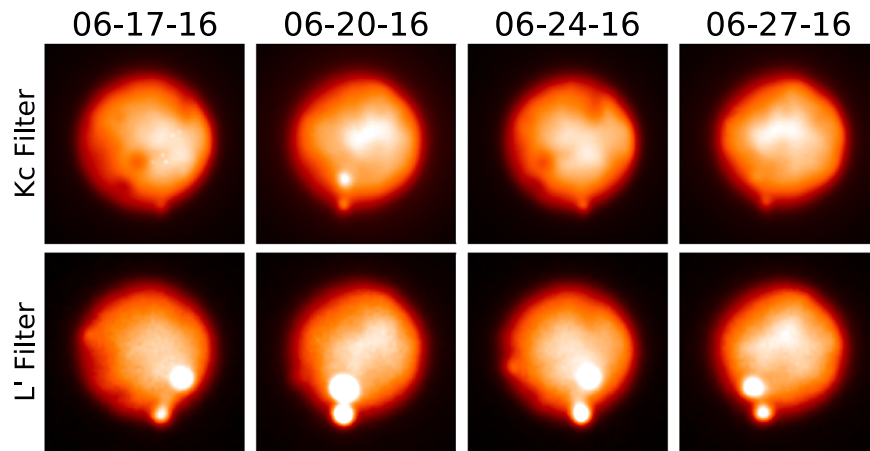


**Figure 3.** Near-infrared images from Gemini N of eruptions in Io’s southern hemisphere in 2016. The hot spot near the south pole is at a new site in the Illyrikon Regio. Despite the apparent similarity between all four  $L'$  images, the viewing geometry changes significantly between observations: from left to right the central meridian longitudes are 249°; 138°; 233°; and 123°W. The mid-latitude hot spot is Marduk Fluctus on June 17 and 24, and is Shamash Patera on June 20 and 27.

**Table 2**  
Bright Eruptions<sup>a</sup>, 2013–2018

Site	Date of Peak (UT)	Lat (°N)	Lon (°W)	$I_{\max,Lp}$ ( $\text{GW } \mu\text{m}^{-1} \text{sr}^{-1}$ )	References
Heno Patera	2013 Aug 15	−56	308	$270 \pm 70$	(c)
Rarog Patera	2013 Aug 15	−39	305	$325 \pm 80$	(c)
Loki Patera <sup>b</sup>	2013 Aug 22	13	308	$136 \pm 20$	(c)
201308C	2013 Aug 29	29	228	>500	(d)
Chors Patera	2014 Oct 22	65	246	$57 \pm 19$	(e)
Mithra Patera	2015 Jan 10	−58	266	$55 \pm 12$	(e)
Sethlaus/Gabija Paterae	2015 Jan 4	−50	198	$33 \pm 5$	(e)
Kurdalagon <sup>b</sup>	2015 May 4	−49	217	$68 \pm 11$	(e)
Amaterasu Patera	2015 Dec 25	39	304	$43 \pm 6$	(e)
P95	2016 May 17	−10	128	$58 \pm 13$	
Shamash Patera	2016 Jun 20	−33	151	$53 \pm 9$	
Illyrikon Regio	2016 Jun 27	−71	180	$125 \pm 69$	
P13	2017 Feb 5	14	229	$23 \pm 2$	
Marduk Fluctus <sup>b</sup>	2017 Feb 5	−24	211	$27 \pm 2$	
Pillan Patera <sup>b</sup>	2017 Feb 23	−11	244	$27 \pm 5$	
Susanoo/Mulungu Paterae	2018 Jan 12	19	221	$20 \pm 3$	
UP 254W	2018 May 10	−37	252	$134 \pm 24$	
Isum Patera	2018 May 27	31	205	$64 \pm 16$	

#### Notes.

<sup>a</sup> All eruptions detected with  $I_{\max,Lp} > 20 \text{ GW } \mu\text{m}^{-1} \text{sr}^{-1}$  during this time period.

<sup>b</sup> Nearly all bright eruptions were transient events at sites where activity was not otherwise detected. Exceptions are Pillan Patera, Loki Patera, and Marduk Fluctus, which were persistently active but exhibited spikes in activity; and Kurdalagon Patera, which was not detected prior to its first eruption but remained detectable afterwards.

**References.** (c) de Pater et al. (2014); (d) de Kleer et al. (2014); (e) de Kleer & de Pater (2016a).

The hot spot was detected again on May 31 but had dimmed nearly to invisibility, and was not seen again. Although the hot spot location is close to the hot spot we refer to as “SE of Pele,” these hot spots are clearly distinct and are spatially resolved in the May 31 observations. No prior activity at this location has been documented.

#### 3.1.4. Eruption at Isum Patera (2018 May–June)

Of the high-power events detected in 2016–2018, the most dramatic in both temperature and duration was an eruption at Isum Patera in 2018 May–June. The event began prior to May 27 and exhibited temperatures around or above 1000 K for the subsequent month. The total emission decayed steadily over

this period, suggesting that new magma was being erupted throughout but at a rate that decreased with time. Figures 4 and 5 show images of the eruption and plot its infrared timeline and the corresponding temperature fits.

#### 3.2. Activity at New Hot Spots

Many of Io’s most active hot spots today have exhibited persistent or episodic activity back to the *Voyager* and *Galileo* missions, nearly 40 yr in some cases. However, the detection of new hot spots at locations where no thermal emission was previously seen is also common in the ground-based data sets (de Pater et al. 2016; Cantrall et al. 2018), including hot spots where no corresponding surface features are seen. The

**Table 3**  
High-temperature Eruptions<sup>a</sup>, 2013–2018

Site	Date (UT)	$\mu$	$T^b$ (K)	References
Shamash Patera	2016 Jun 20	0.81	1000 ± 110	
	2016 Jun 27	0.74	850 ± 80	
Culann	2017 Jun 16	0.81	860 ± 140	
UP 254W	2018 May 10	0.63	960 ± 100	
PV170	2014 Dec 2	0.42	850 ± 40	(c)
Isum Patera	2018 May 27	0.48	1200 ± 220	
	2018 May 31	0.70	1180 ± 120	
	2018 Jun 16	0.84	1120 ± 100	
	2018 Jun 18	0.43	1440 ± 410	
	2018 Jun 23	0.85	980 ± 70	
	2018 Jun 25	0.62	1230 ± 280	
	2018 Jun 30	0.85	1010 ± 80	
PFd1691	2018 Jan 19	0.98	830 ± 80	
Rarog Patera	2013 Aug 15	0.60	1300 ± 200	(d)
	2014 Feb 10	0.78	890 ± 120	(c)
	2015 Mar 31	0.76	950 ± 60	(c)
PV59	2014 Oct 31	0.59	950 ± 200	(c)
P95	2016 May 17	0.39	1020 ± 180	
Kurdalagon Patera	2015-Jan-26	0.54	1200 ± 150	(c)
	2015 Mar 31	0.26	820 ± 110	(c)
	2015 Apr 5	0.57	1300 ± 200	(c)
Tawhaki Patera	2014 Mar 11	0.54	900 ± 170	(c)
	2018 Jan 19	0.97	800 ± 90	
P197	2014 Mar 11	0.67	1000 ± 250	(c)
N Lerna Regio	2014 Dec 2	0.50	820 ± 180	(c)
	2015 Mar 31	0.54	940 ± 120	(c)
Reiden Patera	2017 Dec 12	0.90	1170 ± 100	
201308C	2014 Dec 2	0.64	850 ± 160	(e)
SE of Pele	2017 Dec 12	0.79	950 ± 160	
P123	2015 Jan 11	0.74	820 ± 160	(c)
Illyrikon Regio	2016 Jun 20	0.24	1210 ± 690	
	2016 Jun 27	0.17	1060 ± 340	

#### Notes.

<sup>a</sup> All eruptions detected with  $T > 800$  K during this period.

<sup>b</sup> Temperatures are derived from intensities corrected for geometric foreshortening, and may be overestimated in observations with high emission angle ( $\mu$ ) if fire fountaining is producing a substantial fraction of the short-wavelength emission.

**References.** (c) de Kleer & de Pater (2016a); (d) de Pater et al. (2014); (e) de Kleer et al. (2014).

detection of these new hot spots improves our understanding of the distribution of active volcanic centers on Io's surface and of their heat flow.

Cantrall et al. (2018) identified 24 hot spots that had been detected in ground-based data and were not seen by *Galileo*, more than a quarter of the total number of hot spots seen in the ground-based data set. The new data presented here bring the total number of hot spots seen in the ground-based adaptive optics data sets from 2001–2018 to 104, 29 of which were not seen by previous spacecraft missions. In the new data presented here, the hot spots where thermal emission had not been previously detected were Ekhi Patera, the hot spot in Illyrikon Regio, an unknown location near 54°N 218°W, the hot spot SE of Pele, and an unnamed patera near 37°S 254°W. Of these five, emission from Ekhi Patera and the unknown location at 218°W was detected only once and at low brightness; the hot spot SE of Pele was consistently detected from 2016 December through the end of 2018 though at a low level; and the hot spots

in Illyrikon Regio and at 254°W were locations where bright eruptions took place.

Of the 75 hot spots detected in 2013–2018, about one-third of them were detected throughout the period of observation, one-third were detected only in 2013–2015, and one-third were detected only in 2016–2018. For the set of hot spots that were only detected during one of the two intervals of observation, the majority were detected less than half a dozen times. This characteristic, in combination with the fact that a substantial fraction of these hot spots were previously detected by *Galileo* or *Voyager*, suggests that despite the apparent turnover in activity between observing intervals, it is likely that nearly all hot spots have been geologically active throughout the period of space- and Earth-based observation, but that they only output surface thermal emission sporadically, so that the set of hot spots detected in an observation period may depend heavily on the exact timing of the observations.

A clear exception to this is the category of hot spots where no previous thermal emission has been seen, no clear patera feature is present at the site of the emission, and yet the hot spot stays persistently active for years after the activity is first seen. In this data set, the two most prominent examples are the hot spot in Chalybes Regio, and the hot spot SE of Pele. These appear to be locations where volcanic activity initiated since the *Galileo* mission.

Chalybes Regio is a northern region with extensive lava flow fields. Thermal emission was first detected from this location in 2010 (de Pater et al. 2014), and was attributed to PFu 2083, a small patera floor unit identified by Williams et al. (2011b) at 56°N 74°W. Thermal emission from this location was consistently detected in every observation we made between 2013 and 2018 that had appropriate viewing geometry. In many cases the emission appears spatially extended, indicative of multiple active areas that are not spatially resolved in the data.

The hot spot SE of Pele, located near 35°S 240°W, was first detected on 2016 December 23 and was thereafter detected through the end of our observation period in mid-2018. While there are many flows and paterae in this general area of Io's surface, there is no patera whose location provides a good match to the observed thermal emission.

### 3.3. Persistent Volcanoes and Periodicities

The sites that were most consistently detected during our campaign were Loki Patera (113 detections), Marduk Fluctus (87 detections), Janus Patera (84 detections), the hot spot in Chalybes Regio (80 detections), and Uta (57 detections). The first four of these were detected every time the viewing geometry was favorable. The hot spot at Uta does not appear to stay localized to the patera and may in fact be composed of multiple closely spaced volcanic centers not clearly resolved from one another. The timelines for these five hot spots are shown in Figure 6. The large number of observations of each of these hot spots provides a database of thermal brightness that may be used to fit models for volcanic activity style. In addition, the quantity and cadence of the images result in a data set that is sensitive to periodicities in volcanic brightness on timescales from days to months. The tidal forcing that both powers the activity and deforms Io's crust is periodic, and the resultant activity may reflect these periodicities depending on the rheology and eruption mechanism.

We conducted a periodicity analysis on the five persistently active hot spots listed above by calculating Lomb–Scargle

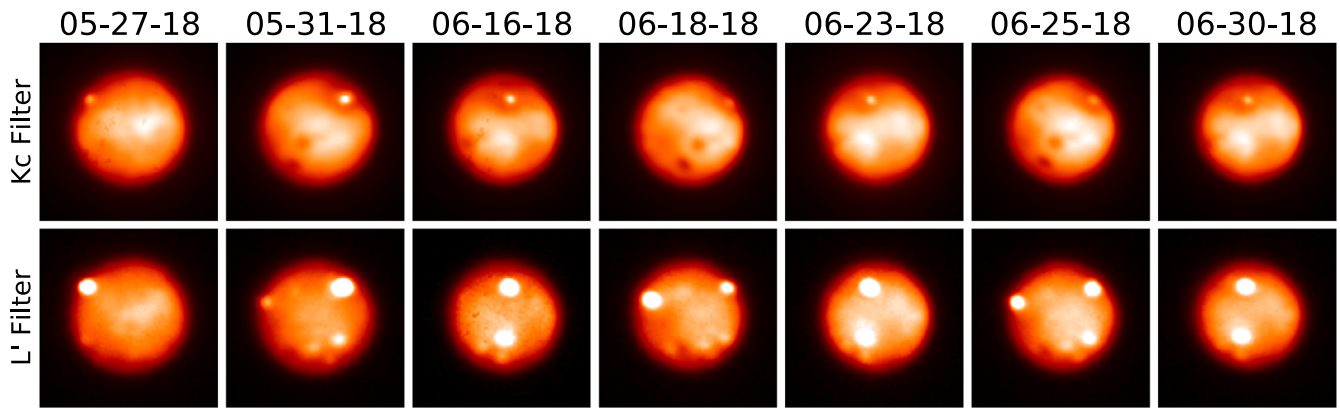


**Figure 4.** Near-infrared images from Gemini N of the eruption at Isum Patera in spring 2018. The eruption is the only hot spot visible in the *K* filter ( $2.27 \mu\text{m}$ ), and is seen at a corresponding location in the *L'* images ( $3.78 \mu\text{m}$ ). The bright hot spot south of Isum Patera is Marduk Fluctus.

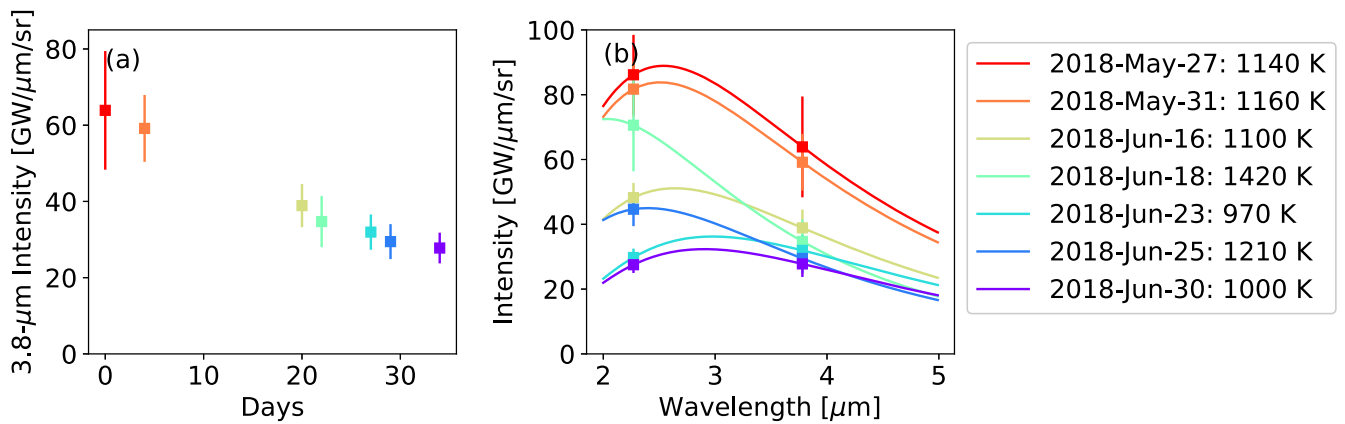


**Figure 5.** Eruption at Isum Patera in 2018. (a) Timeline of  $3.8 \mu\text{m}$  intensity over an  $\sim 1$  month period; (b) temperature fits to the  $2.3$  and  $3.8 \mu\text{m}$  measured brightnesses. Temperatures may be overestimated if lava fountaining is occurring, as discussed in the text.

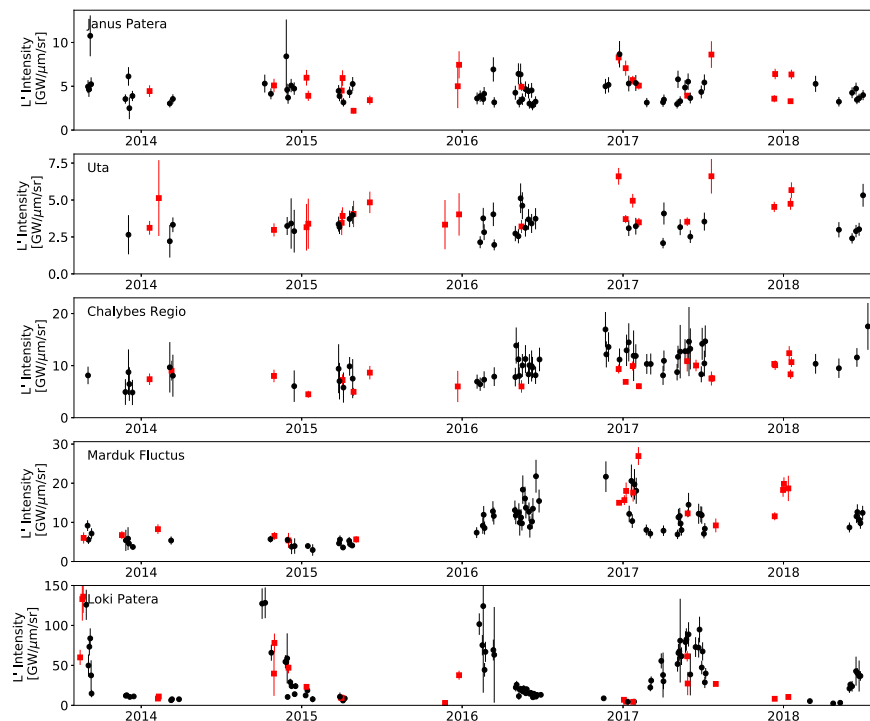


**Figure 6.** Activity timelines for five persistently active hot spots. Black circles and red squares indicate detections with Gemini N and Keck respectively.

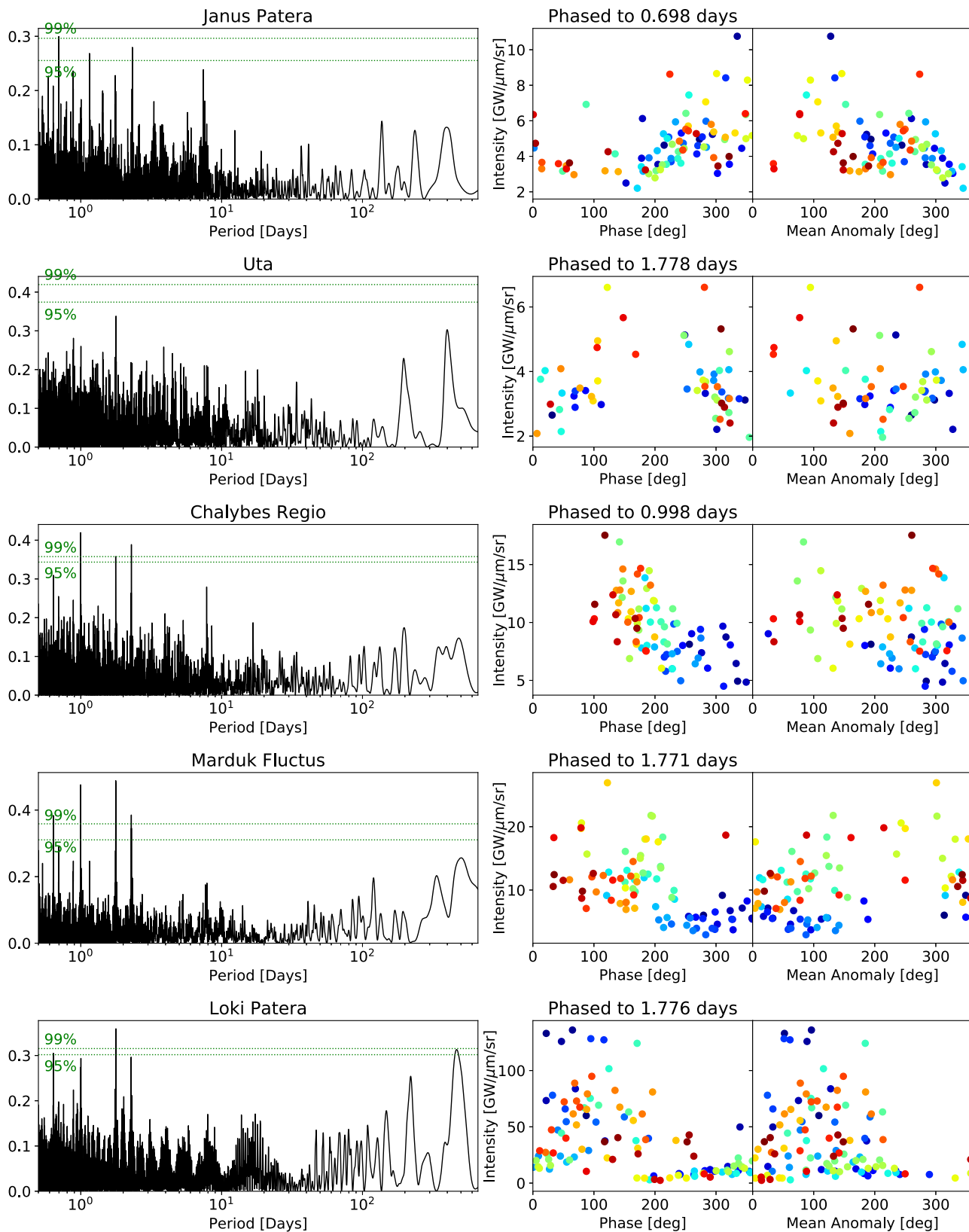


**Figure 7.** Generalized Lomb–Scargle periodograms for the five most consistently detected hot spots. The 99% and 95% significance levels are shown as dotted horizontal lines. The plots in the middle column show the data phased to the period corresponding to the peak in the periodogram, and the rightmost column shows the data as a function of Io’s mean anomaly at the time of observation. The most prominent periodicities are near Io’s and Earth’s rotation periods (1 and 1.77 days), and their beat frequencies (periods near 0.6 and 2.3 days). The mean anomaly plots demonstrate that the 1.77 day periodicities are more consistent with being an observing cadence effect rather than a physical effect due to tidally modulated volcanism, which would exhibit a shorter period and a mean anomaly correlation. Within a given plot, the coloring of points is monotonic with time (blue = earliest; red = latest) to indicate the temporal ordering of the data points.

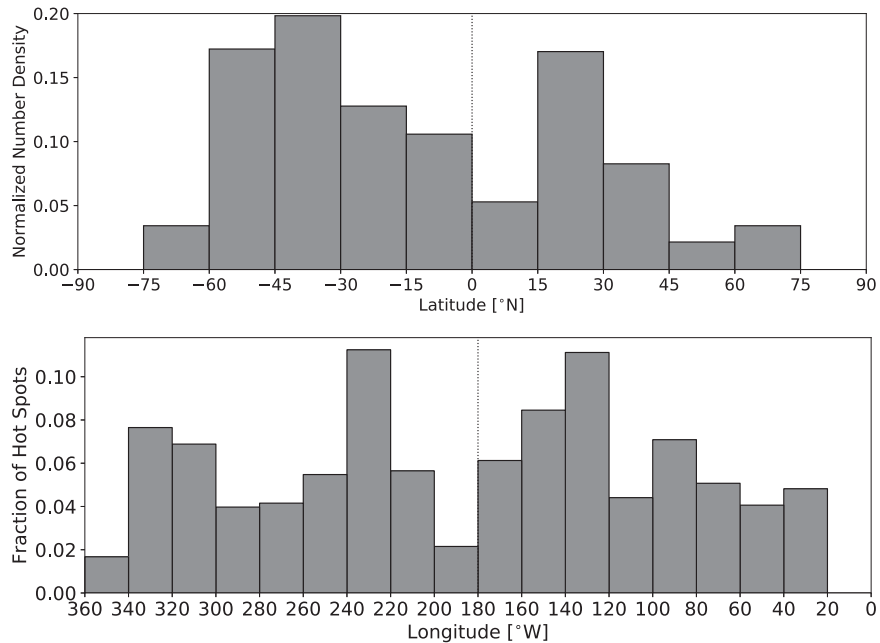


**Figure 8.** Distribution of detected hot spots in latitude and longitude. The longitude distribution is plotted as fraction of total hot spot number per longitude bin, using only hot spots that were detected at  $L'$ , and is corrected for observational biases. The latitude distribution is corrected for the surface area in each latitude bin and normalized but is not corrected for observational biases, which contribute to the dearth of hot spots at high latitudes.

periodograms (Scargle 1982; Zechmeister & Kürster 2009) and comparing the periodogram peaks against significance levels derived by bootstrapping. These periodograms are shown, with significance levels indicated, in Figure 7, and the volcano intensity timeline is plotted phased on the period corresponding to the periodogram peak. The bootstrapping technique samples from the data set randomly with replacement and computes the periodogram; the confidence levels correspond to the percentage of resampled data sets that show no peaks above the indicated level (Ivezić et al. 2014; VanderPlas 2018). Note that because the duration of Io’s eruptions is typically longer than the interval between observations, confidence intervals derived from random resampling will lead to an apparent enhancement in the significance of observing cadence periodicities.

Nearly all hot spots show peaks near 0.997 and 1.77 days, with weaker signals near 0.64 and 2.3 days (seen prominently in many of the periodograms in Figure 7), which correspond to Earth’s sidereal day, Io’s rotation period (sidereal period = 1.7691 days), and the periods corresponding to their beat frequencies ( $\nu_{\text{beat}} = |\nu_1 - \nu_2|$ ). These periods reflect the observing cadence: the average interval between observations is a multiple of Earth’s sidereal day, while repeat observations of a given hot spot are made (on average) at multiples of Io’s rotation period. Io’s rotation period as observed from Earth differs slightly from its sidereal period due to the relative motion of Earth and Jupiter, and is minimized at opposition when the motion of Earth relative to Jupiter is maximized perpendicular to the line of sight. This leads to Earth-apparent rotation periods in the range of 1.7680–1.7691 days.

A periodicity at Io’s rotation period could also be an indication of a tidally modulated volcanic process, whereby the volcanic activity or thermal emission is controlled in part by diurnally varying tidal stresses. However, the periodicities near Io’s rotation period in the data set analyzed here do not show evidence for this effect. In particular, the peak periodogram power is at periods of 1.769–1.776 days, which match or

slightly exceed Io’s apparent rotation period but are a poorer match to Io’s 1.7627 day anomalistic period, or time between successive perijoves, which is the relevant parameter for diurnal stresses and differs from the apparent rotation period due to the precession of Io’s orbit. In order to further highlight the difference between the observed 1.77 day signal and Io’s tidal forcing, the rightmost column in Figure 7 shows the brightness of each volcano as a function of Io’s mean anomaly at the time of observation, demonstrating that there is no mean anomaly correlation even in hot spots that show a strong 1.77 day periodicity.

The period of precession of Io’s longitude of perijove is  $\sim 1.5$  yr, so that on the timescale of a few months we see the same Ionian longitudes near a similar phase of Io’s orbit, which likely accounts for the prominence of both Earth’s and Io’s rotation periods in the periodograms. This can be seen in the middle column of Figure 7: all data points are color-coded by time (cycling from blue to red from early to late), and it is clear from the middle plot of the Chalybes Regio panel, for example, that the apparent periodicity likely arises from a combination of a long-term brightening and observing cadence biases. In essence, we are unable to rigorously distinguish between a scenario where a volcano is variable over an orbital period, and a scenario where it is variable over a longer timescale but observational effects caused apparent orbital-timescale periodicities.

This limitation could be entirely eliminated in a spacecraft data set, where the observing cadence is less regular and the same hot spot can be viewed at a variety of mean anomalies within a time period that is short relative to the timescale for intrinsic variability of that volcano.

Only Loki Patera shows a statistically significant periodicity at a period other than the four discussed above. Over the time period of observation analyzed here, Loki Patera’s activity was periodic with a period of 465.63 days.

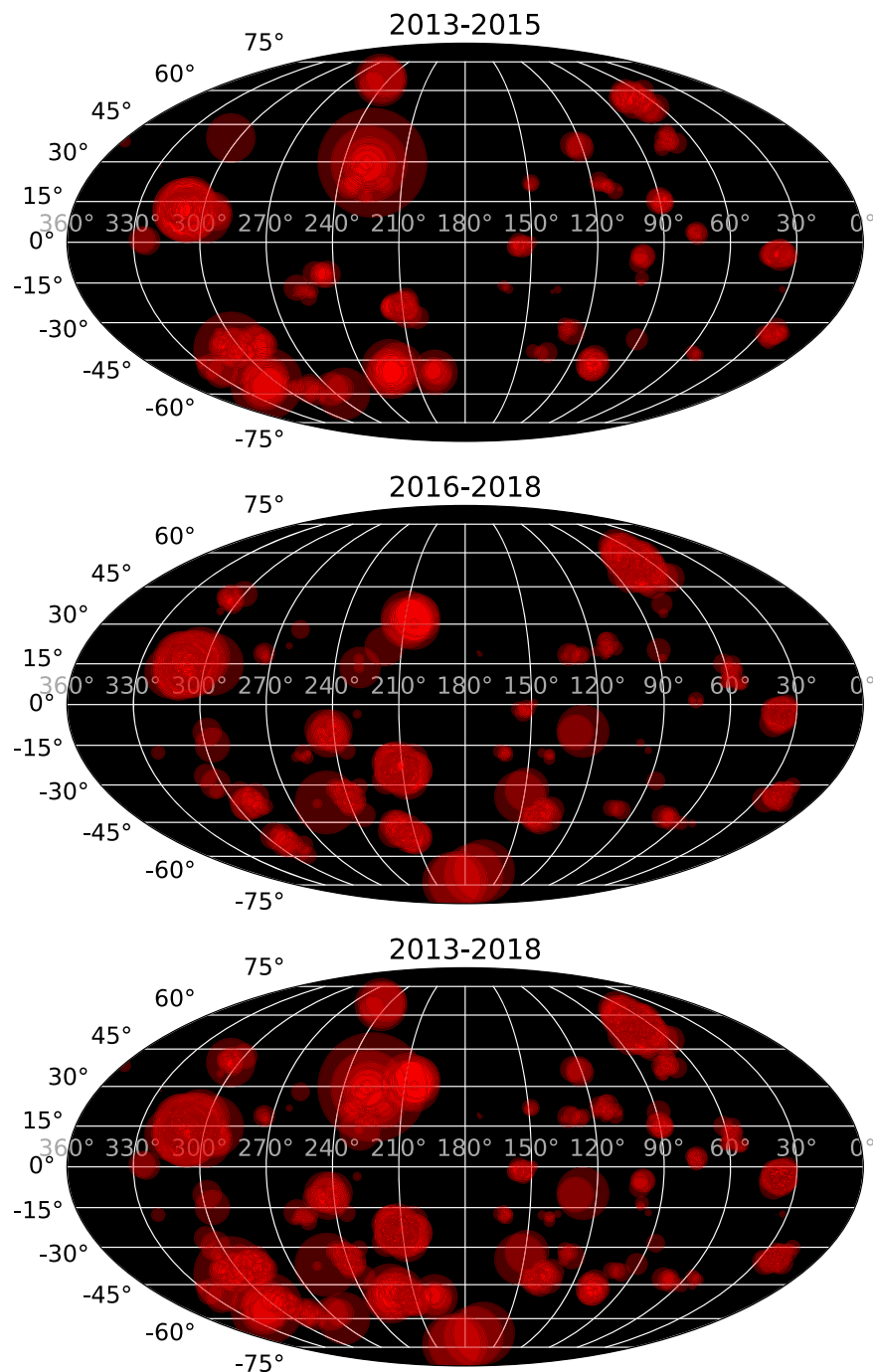


**Figure 9.** Spatial distribution of hot spot thermal emission detected on Io in 2013–2018. Each circle shows the location and brightness of a single hot spot detection, with circle size proportional to the log of the  $3.8\ \mu\text{m}$  intensity. All circles are semi-transparent, and high-opacity regions indicate multiple detections at the same location. The top and middle panels show the distribution in two distinct time periods (the 2013–2015 plot is identical to that given in de Kleer & de Pater 2016a), and the bottom panel shows the cumulative distribution from 2013 to 2018. The position uncertainties are typically a few degrees at low latitudes and higher toward the poles; much but not all of the apparent jitter in hot spot locations is within these uncertainties.

### 3.4. Hot Spot Spatial Distribution

The distribution of hot spot number density with latitude and longitude is shown in Figure 8, and Figure 9 plots the location and brightness of all  $L'$ -band hot spot detections, updated from a similar figure based on the 2013–2015 data in de Kleer & de Pater (2016b). The longitudinal distribution has been corrected for the sensitivity of the observations to each longitude bin. The latitudinal distribution is not corrected because the latitudinal differences in the volcano brightness distribution or in topography are poorly constrained.

Our observations in 2013–2015 showed an apparent difference in the spatial distribution of bright, transient eruptions compared to persistent hot spots (de Kleer & de Pater 2016b). In particular, all nine of the volcanoes that hosted bright eruptions ( $I_{\text{max},Lp} > 30\ \text{GW}\ \mu\text{m}^{-1}\ \text{sr}^{-1}$ ) during those years are located on the trailing hemisphere. In the full data set (2013–2018), 18 volcanoes exhibited bright eruptions, where bright is defined as  $I_{\text{max},Lp} > 20\ \text{GW}\ \mu\text{m}^{-1}\ \text{sr}^{-1}$ . Note that this definition is effectively the same as in our previous paper because there were no volcanoes with detected  $I_{\text{max},Lp}$  between 20 and  $30\ \text{GW}\ \mu\text{m}^{-1}\ \text{sr}^{-1}$  in 2013–2015.

The threshold was lowered because the larger data set now available indicates that no volcano persistently maintains a flux density level above  $20 \text{ GW } \mu\text{m}^{-1} \text{ sr}^{-1}$ , and this cutoff is therefore sufficient to isolate bright transient events. Of these 18 volcanoes, every single one falls within a  $180^\circ$  band in longitude, from  $128$  to  $308^\circ\text{W}$ , despite the fact that our program had comparable sensitivity to events of this magnitude at all Ionian longitudes. Moreover, all but two of the eruptions occurred on Io's trailing hemisphere ( $180$ – $360^\circ\text{W}$ ); the probability of 16 or more eruptions occurring on the trailing hemisphere (given 18 eruptions total) is 0.00066 if volcanoes are randomly distributed in longitude.

Despite the distinctive distribution of the largest eruptions, there is no significant difference between the two hemispheres in terms of spatially and temporally averaged near-infrared brightness (provided that Loki Patera is excluded), nor in the number of active hot spots. The time-averaged volcanic  $L'$ -band intensity arises 47.5% and 52.5% from the leading and trailing hemispheres, respectively (excluding Loki Patera), while the number of hot spots detected at  $L'$  is identical between the two hemispheres (31 hot spots, excluding those detected only at longer wavelengths, to which only a subset of the data were sensitive).

In order to further explore whether any hemispheric-scale asymmetries are present in the distribution of the hot spots, we broaden this analysis from a comparison of just leading versus trailing hemispheres by choosing all  $180^\circ$  longitude intervals and determining the fraction of hot spots that fall within each interval. While the leading and trailing hemispheres exhibit comparable time-averaged radiances and hot spot number, there is an asymmetry between the sub- and anti-Jovian hemispheres with more hot spots and higher radiances on the anti-Jovian hemisphere, despite the fact that this hemisphere had poorer coverage during our program. The hemisphere centered on  $160^\circ\text{W}$  maximizes both metrics, containing  $\sim 60\%$  of the hot spots and  $>70\%$  of the time-averaged radiances. However, in artificial data sets where hot spots are randomly distributed in longitude, an asymmetry in hot spot number at this level is well within the expected range (i.e., within one  $\sigma$  of the median).

#### 4. Conclusions

We present results from measurements of the thermal emission of Io's volcanoes, derived from near-infrared imaging with adaptive optics at the Keck and Gemini N telescopes on 271 nights between 2013 August and the end of 2018. The first 100 nights of observations were presented in de Kleer & de Pater (2016a), while the 171 nights since the start of 2016 are presented here for the first time. Over the five years of the program to date, we made 980 detections of over 75 unique hot spots, with some hot spots detected more than 80 times and Loki Patera detected 113 times. We provide downloadable tables of hot spot brightnesses and observing details, and hope that these data products will serve as a resource for others in the community who will build on the analyses presented here.

Nearly all bright transient eruptions where temperature measurements were possible displayed temperatures above 800 K, confirming that eruptions at such high temperatures are common and are likely the rule rather than the exception. The detection of new hot spots that were not previously detected by spacecraft is a common occurrence. Adding the data presented here to that summarized by Cantrall et al. (2018), there have now been 104 distinct hot spots seen in the AO data from 2001–2018, 25–30 of which were not previously seen by spacecraft. It is

likely that many of these hot spots have been active since before the *Galileo* and *Voyager* visits but were not emitting sufficient radiation during the visits to have been detected. However, some of the new hot spots have no corresponding surface feature and remain persistently active after they are first detected (e.g., Chalybes Regio and the hot spot SE of Pele), suggesting that activity recently initiated at these locations. We performed a periodicity search on the five most consistently detected hot spots (each detected 57–113 times) but did not detect any new periodicities beyond those introduced by the observing cadence. Spacecraft data would be needed to draw a robust conclusion about tidally modulated volcanism on diurnal timescales.

de Kleer & de Pater (2016b) noted that all bright, transient eruptions took place on Io's trailing hemisphere. This trend continues through the additional 3 yr of data presented here, and the probability of the observed asymmetry is 0.00066 if volcanoes are randomly distributed. Note that this asymmetry applies only to the character of the volcanism; the number and cumulative near-IR radiance is nearly identical between leading and trailing hemispheres.

This data set now constitutes the largest set of unique detections of thermal emission from individual Ionian hot spots to date, permitting robust statistical analyses of properties such as the spatial distribution of hot spot activity, the variability and time-averaged power of numerous individual hot spots, and the occurrence rates of bright and/or high-temperature eruptions. These data, in combination with *Galileo's* sensitivity to smaller, cooler hot spots and the multidecadal time baseline provided by ground-based occultation data, are now providing a truly global, multiwavelength picture of Io's volcanic activity over a wide range of timescales.

The timing of our program coincided with intensive observations of the extended sodium cloud and the plasma torus by ground-based programs and by the *EXCEED/Hisaki* and *Juno* missions. The correlation of these data sets with our timeline of Io's activity is already providing clues into the connections between different components of the Jovian system (Yoshikawa et al. 2017; Koga et al. 2018; Morgenthaler et al. 2019), but our understanding of this system is far from complete. Continued coverage of Io's volcanoes throughout these missions will be key to unraveling the sources of variability in the Jovian neutral and plasma environment.

K.d.K. is supported by the Heising-Simons Foundation through a *51 Pegasi b* postdoctoral fellowship, and this research was partially supported by the National Science Foundation grant AST-1313485 to UC Berkeley and a NASA Keck PI Data Award, administered by the NASA Exoplanet Science Institute. We are grateful to Roy and Frances Simperman for their support of the Keck Visiting Scholars program, which enabled K.d.K., E.M., and C.A. to develop the Keck twilight program through which some of the data presented here were obtained. We thank G. Puniwai for acquiring several of the Keck observations. We thank P. Capak, J. Cohen, N. Harnitschek, D. Masters, and S.A. Stanford of the the Complete Calibration of the Color-Redshift Relation (C3R2; Masters et al. 2017) NASA Keck Key Strategic Mission Support survey team for providing twilight observations on the nights of UT 2017 December 11–13. The work of D.S. and A.G.D. was carried out at the Jet Propulsion Laboratory, California Institute of Technology, under a contract with NASA. Much of the data presented herein were obtained at the Gemini Observatory, which is operated by the Association of Universities for Research in

Astronomy, Inc., under a cooperative agreement with the NSF on behalf of the Gemini partnership: the National Science Foundation (United States), National Research Council (Canada), CONICYT (Chile), Ministerio de Ciencia, Tecnología e Innovación Productiva (Argentina), Ministério da Ciência, Tecnologia e Inovação (Brazil), and Korea Astronomy and Space Science Institute (Republic of Korea). Some of the data presented herein were obtained at the W. M. Keck Observatory, which is operated as a scientific partnership among the California Institute of Technology, the University of California and the National Aeronautics and Space Administration. Some of the data was obtained at the W. M. Keck Observatory from telescope time allocated to the National Aeronautics and Space Administration through the agency’s scientific partnership with the California Institute of Technology and the University of California. The Observatory was made possible by the generous financial support of the W. M. Keck Foundation. The authors wish to recognize and acknowledge the very significant cultural role and reverence that the summit of Maunakea has always had within the indigenous Hawaiian community. We are most fortunate to have the opportunity to conduct observations from this mountain.

### Appendix Tables

Table 4 provides details on the observations, and Table 5 provides the measured intensities for all hot spot detections in

2013–2018, corrected for geometric foreshortening. Both Tables 4 and 5 are available for download.

**Table 4**  
Observations

Date <sup>a</sup> (UT)	Tel/Inst	Lon <sup>b</sup> (°W)	Lat <sup>b</sup> (°N)	Distance <sup>b</sup> (au)
2013 Aug 15	Keck/NIRC2	337.0	2.0	5.85
2013 Aug 20	Keck/NIRC2	275.0	2.0	5.79
2013 Aug 21	Keck/NIRC2	115.0	2.0	5.78
2013 Aug 22	Keck/NIRC2	319.0	2.0	5.77
2013 Aug 23	Keck/NIRC2	161.0	2.0	5.76
2013 Aug 29	Gemini N/NIRI	305.7	1.9	5.69
2013 Aug 30	Gemini N/NIRI	146.2	1.9	5.68
2013 Sep 1	Gemini N/NIRI	192.7	1.9	5.65
2013 Sep 2	Gemini N/NIRI	36.4	1.9	5.65
2013 Sep 3	Gemini N/NIRI	241.4	1.9	5.63

**Notes.**

<sup>a</sup> Data from 2013 August 15 to 23 were previously published in de Pater et al. (2014) and data from 2013 to 2015 were previously published in de Kleer & de Pater (2016a).

<sup>b</sup> Sub-observer latitude and longitude, and Earth-Io distance, from JPL Horizons.

(This table is available in its entirety in machine-readable form.)

**Table 5**  
Hot Spot Intensities<sup>a</sup>

Hot Spot	Date (UT)	Lat (°N)	Lon (°W)	$K$ -cont $\lambda = 2.27 \mu\text{m}$	$\text{H}_2\text{O}$ $3.06 \mu\text{m}$	PAH $3.29 \mu\text{m}$	$L'$ $3.78 \mu\text{m}$ ( $\text{GW } \mu\text{m}^{-1} \text{sr}^{-1}$ )	$\text{Br}\alpha$ -cont $3.99 \mu\text{m}$	$\text{Br}\alpha$ $4.05 \mu\text{m}$	$M_s$ $4.67 \mu\text{m}$
Nusku Patera	2017 May 27	$-65.0 \pm 1.1$	$6.2 \pm 1.9$						$4.0 \pm 1.0$	
	<b>Average</b>	<b>-65.0</b>	<b>6.2</b>							
Uta	2013 Dec 3	$-33.8 \pm 2.0$	$20.1 \pm 2.1$				$2.7 \pm 1.3$			
	2014 Jan 20	$-34.9 \pm 0.8$	$20.9 \pm 0.8$			$1.6 \pm 0.2$	$3.1 \pm 0.5$			$5.4 \pm 0.8$
	2014 Feb 10	$-34.1 \pm 0.5$	$23.4 \pm 2.1$				$5.1 \pm 2.6$			$4.6 \pm 0.9$
	2014 Mar 7	$-34.9 \pm 2.0$	$25.9 \pm 2.2$				$2.2 \pm 1.1$			
	2014 Mar 14	$-34.7 \pm 2.0$	$24.8 \pm 2.1$				$3.3 \pm 0.5$			
	2014 Oct 30	$-33.7 \pm 0.8$	$21.2 \pm 0.8$				$3.0 \pm 0.4$			$5.8 \pm 0.9$
	2014 Nov 29	$-35.5 \pm 2.1$	$20.6 \pm 2.1$				$3.2 \pm 0.6$			
	2014 Dec 8	$-34.1 \pm 1.6$	$19.1 \pm 2.5$				$3.4 \pm 1.7$			
	2014 Dec 15	$-34.2 \pm 1.8$	$19.6 \pm 2.3$				$2.9 \pm 1.4$			
	2015 Jan 12	$-35.4 \pm 1.0$	$22.6 \pm 1.8$				$3.2 \pm 1.6$			$4.9 \pm 0.7$
	2015 Jan 16	$-34.1 \pm 1.0$	$21.0 \pm 1.8$				$3.4 \pm 1.7$			$4.6 \pm 0.7$
	2015 Mar 26	$-37.0 \pm 2.0$	$22.1 \pm 2.2$				$3.4 \pm 0.5$			
	2015 Mar 28	$-34.6 \pm 1.8$	$25.3 \pm 2.3$				$3.2 \pm 0.5$			
	2015 Apr 2	$-33.5 \pm 0.6$	$23.9 \pm 1.3$				$3.5 \pm 0.8$			$4.7 \pm 0.7$
	2015 Apr 4	$-33.9 \pm 0.5$	$24.8 \pm 0.5$				$3.9 \pm 0.6$			$6.1 \pm 0.9$

**Table 5**  
(Continued)

Hot Spot	Date	Lat	Lon	$K$ -cont $\lambda = 2.27 \mu\text{m}$	$\text{H}_2\text{O}$ $3.06 \mu\text{m}$	PAH $3.29 \mu\text{m}$	$L'$ $3.78 \mu\text{m}$ ( $\text{GW } \mu\text{m}^{-1} \text{sr}^{-1}$ )	Br $\alpha$ -cont $3.99 \mu\text{m}$	Br $\alpha$ $4.05 \mu\text{m}$	$M_S$ $4.67 \mu\text{m}$
	(UT)	( $^\circ\text{N}$ )	( $^\circ\text{W}$ )							
	2015 Apr 20	$-34.6 \pm 1.9$	$27.2 \pm 2.2$				$3.7 \pm 0.6$			
	2015 Apr 27	$-35.8 \pm 2.0$	$24.4 \pm 2.1$				$4.0 \pm 0.6$			
	2015 Apr 29	$-34.7 \pm 0.7$	$23.4 \pm 1.2$				$4.1 \pm 0.9$			$5.4 \pm 0.8$
	2015 Jun 5	$-32.2 \pm 0.7$	$23.5 \pm 0.9$			$3.3 \pm 0.5$	$4.8 \pm 0.7$			$7.1 \pm 1.1$
	2015 Nov 23	$-35.5 \pm 0.7$	$21.3 \pm 1.9$				$3.3 \pm 1.7$			$5.2 \pm 0.8$
	2015 Dec 25	$-34.6 \pm 0.6$	$22.7 \pm 1.9$				$4.0 \pm 1.4$			$6.1 \pm 0.9$
	2016 Feb 11	$-32.3 \pm 1.3$	$18.1 \pm 1.8$				$2.1 \pm 0.4$			
	2016 Feb 18	$-31.9 \pm 1.2$	$18.2 \pm 1.3$				$3.8 \pm 0.7$			
	2016 Feb 20	$-32.3 \pm 1.3$	$22.2 \pm 1.9$				$2.8 \pm 0.5$			
	2016 Mar 12	$-35.9 \pm 1.3$	$19.6 \pm 2.8$				$4.0 \pm 0.8$			
	2016 Mar 14	$-32.7 \pm 1.2$	$20.9 \pm 1.3$				$2.0 \pm 0.4$			
	2016 May 1	$-32.0 \pm 1.4$	$19.5 \pm 1.9$				$2.7 \pm 0.5$			
	2016 May 8	$-32.8 \pm 1.4$	$24.1 \pm 1.5$				$2.5 \pm 0.5$			
	2016 May 13	$-34.7 \pm 1.4$	$22.2 \pm 2.8$				$5.1 \pm 1.0$			
	2016 May 15	$-35.4 \pm 0.5$	$23.5 \pm 1.7$			$2.6 \pm 0.4$	$3.2 \pm 0.5$			$5.4 \pm 0.8$
	2016 May 17	$-33.3 \pm 1.4$	$21.0 \pm 2.6$				$4.6 \pm 0.9$			
	2016 May 24	$-31.5 \pm 1.4$	$22.2 \pm 2.0$				$3.1 \pm 0.6$			
	2016 May 31	$-32.0 \pm 1.5$	$21.9 \pm 1.7$				$3.7 \pm 0.7$			
	2016 Jun 7	$-34.7 \pm 1.5$	$24.0 \pm 1.6$				$3.4 \pm 0.6$			
	2016 Jun 16	$-34.9 \pm 1.6$	$18.5 \pm 2.3$				$3.7 \pm 0.7$			
	2016 Dec 22	$-35.3 \pm 1.1$	$20.1 \pm 1.2$			$3.3 \pm 0.5$	$6.6 \pm 1.0$	$7.8 \pm 1.2$	$9.7 \pm 1.5$	$7.5 \pm 1.1$
	2017 Jan 3	$-34.4 \pm 0.9$	$17.9 \pm 1.5$						$8.0 \pm 1.4$	$8.9 \pm 1.3$
	2017 Jan 7	$-35.6 \pm 1.2$	$20.4 \pm 1.5$				$3.7 \pm 0.6$	$5.3 \pm 0.8$	$6.6 \pm 1.5$	$7.0 \pm 1.0$
	2017 Jan 14	$-33.6 \pm 1.5$	$19.6 \pm 1.9$				$3.1 \pm 0.5$			
	2017 Jan 23	$-34.7 \pm 0.7$	$20.6 \pm 1.5$				$5.0 \pm 0.7$			
	2017 Jan 30	$-36.5 \pm 1.5$	$19.1 \pm 2.3$				$3.2 \pm 0.6$			
	2017 Feb 6	$-35.6 \pm 1.0$	$19.2 \pm 0.6$				$3.5 \pm 0.5$	$4.5 \pm 0.7$	$4.7 \pm 0.7$	$7.3 \pm 1.1$
	2017 Apr 2	$-31.5 \pm 1.2$	$19.7 \pm 1.3$				$2.1 \pm 0.4$			
	2017 Apr 4	$-34.4 \pm 1.3$	$21.0 \pm 2.6$				$4.1 \pm 0.7$			
	2017 May 11	$-33.1 \pm 1.3$	$20.3 \pm 1.3$				$3.2 \pm 0.5$			

**Table 5**  
(Continued)

Hot Spot	Date	Lat	Lon	$K$ -cont $\lambda = 2.27 \mu\text{m}$	$\text{H}_2\text{O}$ $3.06 \mu\text{m}$	PAH $3.29 \mu\text{m}$	$L'$ $3.78 \mu\text{m}$ ( $\text{GW } \mu\text{m}^{-1} \text{sr}^{-1}$ )	$\text{Br}\alpha$ -cont $3.99 \mu\text{m}$	$\text{Br}\alpha$ $4.05 \mu\text{m}$	$M_s$ $4.67 \mu\text{m}$
	(UT)	( $^\circ\text{N}$ )	( $^\circ\text{W}$ )							
	2017 May 27	$-34.4 \pm 0.8$	$24.7 \pm 0.8$		$1.1 \pm 0.2$	$2.1 \pm 0.3$	$3.5 \pm 0.5$	$7.0 \pm 1.2$	$9.8 \pm 2.4$	$8.3 \pm 1.2$
	2017 Jun 3	$-34.0 \pm 1.4$	$22.6 \pm 1.6$				$2.5 \pm 0.4$			
	2017 Jul 5	$-34.7 \pm 1.5$	$21.3 \pm 1.9$				$3.5 \pm 0.6$			
	2017 Jul 21	$-35.8 \pm 0.5$	$25.7 \pm 0.7$				$6.6 \pm 1.2$	$7.9 \pm 1.2$		$8.3 \pm 1.2$
	2017 Dec 11	$-33.9 \pm 0.4$	$20.6 \pm 0.3$				$4.5 \pm 0.7$			
	2018 Jan 17	$-33.8 \pm 0.7$	$19.6 \pm 0.8$				$4.7 \pm 0.7$			
	2018 Jan 19	$-36.0 \pm 0.3$	$16.8 \pm 0.0$				$5.7 \pm 0.9$			$9.1 \pm 1.4$
	2018 May 7	$-35.8 \pm 1.3$	$22.0 \pm 2.0$				$3.0 \pm 0.5$			
	2018 Jun 6	$-31.0 \pm 1.2$	$19.7 \pm 1.3$				$2.4 \pm 0.4$			
	2018 Jun 15	$-32.5 \pm 1.3$	$20.0 \pm 1.3$				$2.9 \pm 0.4$			
	2018 Jun 22	$-30.1 \pm 1.2$	$17.9 \pm 1.3$				$3.0 \pm 0.5$			
	2018 Jul 1	$-33.1 \pm 1.3$	$21.3 \pm 1.5$				$5.3 \pm 0.8$			
	<b>Average</b>	<b><math>-34.4</math></b>	<b><math>21.0</math></b>							

**Note.**

<sup>a</sup> All flux densities are corrected for geometric foreshortening. The bold values denote the average latitudes and longitudes of each hot spot.

(This table is available in its entirety in machine-readable form.)

**ORCID iDs**

Katherine de Kleer  <https://orcid.org/0000-0002-9068-3428>

Imke de Pater  <https://orcid.org/0000-0002-4278-3168>

Edward M. Molter  <https://orcid.org/0000-0003-3799-9033>

Ashley Gerard Davies  <https://orcid.org/0000-0003-1747-8142>

Randy Campbell  <https://orcid.org/0000-0002-3289-5203>

Nikole M. Nielsen  <https://orcid.org/0000-0003-2377-8352>

Daniel Stern  <https://orcid.org/0000-0003-2686-9241>

**References**

- Cantrall, C., de Kleer, K., de Pater, I., et al. 2018, *Icar*, **312**, 267
- Carlson, R. W., Weissman, P. R., Smythe, W. D., & Mahoney, J. C. 1992, *SSRv*, **60**, 457
- Carr, M. H. 1986, *JGR*, **91**, 3521
- Davies, A. G. 2007, *Volcanism on Io: A Comparison with Earth* (Cambridge: Cambridge Univ. Press)
- Davies, A. G., Davies, R. L., Veeder, G. J., et al. 2018, *GeoRL*, **45**, 2926
- Davies, A. G., Keszthelyi, L. P., & Harris, A. J. L. 2010, *JVGR*, **194**, 75
- Davies, A. G., Veeder, G. J., Matson, D. L., & Johnson, T. V. 2012, *GeoRL*, **39**, L01201
- de Kleer, K., & de Pater, I. 2016a, *Icar*, **280**, 378
- de Kleer, K., & de Pater, I. 2016b, *Icar*, **280**, 405
- de Kleer, K., de Pater, I., Davies, A. G., et al. 2014, *Icar*, **242**, 352
- de Pater, I., Davies, A. G., Ádámkóvics, M., & Ciardi, D. R. 2014, *Icar*, **242**, 365
- de Pater, I., Davies, A. G., & Marchis, F. 2016, *Icar*, **274**, 284
- Gaskell, R. W., Synnott, S. P., McEwen, A. S., & Schaber, G. G. 1988, *GeoRL*, **15**, 581
- Hamilton, C. W., Beggan, C. D., Still, S., et al. 2013, *E&PSL*, **361**, 272
- Hodapp, K. W., Jensen, J. B., Irwin, E. M., et al. 2003, *PASP*, **115**, 1388
- Ivezić, Ž., Connolly, A. J., VanderPlas, J. T., & Gray, A. 2014, *Statistics, Data Mining, and Machine Learning in Astronomy* (Princeton, NJ: Princeton Univ. Press)
- Johnson, T. V., Veeder, G. J., Matson, D. L., et al. 1988, *Sci*, **242**, 1280
- Koga, R., Tsuchiya, F., Kagitani, M., et al. 2018, *Icar*, **299**, 300
- Lopes-Gautier, R., McEwen, A. S., Smythe, W. B., et al. 1999, *Icar*, **140**, 243
- Marchis, F., de Pater, I., Davies, A. G., et al. 2002, *Icar*, **160**, 124
- Masters, D. C., Stern, D. K., Cohen, J. G., et al. 2017, *ApJ*, **841**, 111
- Morgenthaler, J. P., Rathbun, J. A., Schmidt, C. A., Baumgardner, J., & Schneider, N. M. 2019, *ApJL*, **871**, L23
- Rathbun, J. A., Howell, R. R., & Spencer, J. R. 2018, *LPI*, **49**, 2083
- Rathbun, J. A., & Spencer, J. R. 2010, *Icar*, **209**, 625
- Scargle, J. D. 1982, *ApJ*, **263**, 835
- Segatz, M., Spohn, T., Ross, M. N., Schubert, G., et al. 1988, *Icar*, **75**, 187
- Spencer, J. R., Shure, M. A., Ressler, M. E., et al. 1990, *Natur*, **348**, 618
- Tsang, C. C. C., Rathbun, J. A., Spencer, J. R., Hesman, B. E., & Abramov, O. 2014, *JGRE*, **119**, 2222
- VanderPlas, J. T. 2018, *ApJS*, **236**, 16
- Veeder, G. J., Davies, A. G., Matson, D. L., et al. 2012, *Icar*, **219**, 701
- Veeder, G. J., Matson, D. L., Johnson, T. V., Blaney, D. L., & Goguen, J. D. 1994, *JGRE*, **99**, 17095
- Veeder, G. J., Davies, A. G., Matson, D. L., et al. 2015, *Icar*, **245**, 379
- Williams, D. A., Keszthelyi, L. P., & Crown, D. A. 2011a, *Icar*, **214**, 91
- Williams, D. A., Keszthelyi, L. P., Crown, D. A., et al. 2011b, *USGS*, **3168**
- Wizinowich, P., Acton, D. S., Shelton, C., et al. 2000, *PASP*, **112**, 315
- Yoshikawa, I., Suzuki, F., Hikida, R., et al. 2017, *EP&S*, **69**, 110
- Zechmeister, M., & Kürster, M. 2009, *A&A*, **496**, 577